Development of Tomography Techniques Using a Compact Fast Neutron Generator

R. E. Adams[1,3*], B. P. Soubelet[1], H. Kromer[1,2], R. Zboray[2,**], H. M. Prasser[1,2], V. Petrov[3], A. Manera[3]

[1] ETH Zurich, Department of Mechanical and Process Engineering, Zurich, Switzerland
[2] Paul Scherrer Institute, Nuclear Energy and Safety Research Department, Villigen, Switzerland
[3] University of Michigan, Department of Nuclear Engineering and Radiological Sciences, Ann Arbor MI, USA
[**]Current affiliation: The Pennsylvania State University, Department of Mechanical and Nuclear Engineering, University Park PA, USA

[*]Email: adams@lke.mavt.ethz.ch

ABSTRACT

This work gives an overview of ongoing development of tomography techniques based on a compact fast neutron generator. The three main lines of this work are the source development, detector array development, and studies of novel energy-selective techniques. The source development uses a custom D-D fast neutron generator at the Paul Scherrer Institute specifically designed for imaging applications. The status of the source details and performance are described. A prototype plastic scintillator detector array with a 6 mm pitch was used to produce test tomographic images with a 2 mm resolution using this custom source. A second-generation detector array, with a finer 2.5 mm detector pitch and greatly improved custom readout electronics is also described. This array was tested at first with an Ir-192 gamma source and achieved a spatial resolution of about 1 mm. A unique property of D-D neutron generators is their quasi-monoenergetic neutron output which varies with emission angle. This forms the potential basis of multi-energy imaging, in which specific elements can in principle be identified in a sample. The first feasibility simulations and measurements related to this technique are described. The potential areas of application of this imaging work and its outlook are also given.

Keywords Fast neutron tomography, gamma tomography, scintillator detector array

Industrial Application: General

1 INTRODUCTION

Fast neutrons are highly penetrating and exhibit macroscopic attenuation coefficients which do not strongly vary from one material to another. This makes them an attractive alternative to X-rays when imaging bulky samples, particularly when a low-Z material of interest (e.g. water or oil) is behind a thick high-Z (e.g. steel) structure. In these cases, X-rays and even gamma sources lack penetration through the high-Z material and good contrast in the low-Z material. Compact fast neutron generators based on the D-D fusion reaction provide a quasi-monoenergetic fast neutron flux which can be used for such imaging purposes. They have the further characteristic of emitting neutrons with an energy which varies according to the angle of emission, from roughly 2.2 to 2.8 MeV for typical operating conditions, as shown in Figure 1. This means that, depending on the emission angle used, a different energy can be chosen for imaging. Fast neutron cross-sections are uniquely material and energy dependent, meaning that performing tomographic imaging at multiple energies (i.e., multiple source emission angles) can in principle provide multiple local attenuation values which can be used to identify specific materials. This is unlike X-ray or gamma attenuation coefficients, which are predominately Z-dependent and therefore difficult to distinguish when both Z-value and density are varying. An overview of the attenuation coefficients of several typical materials over the energy ranges of interest for neutrons and photons is shown in Figure 1.

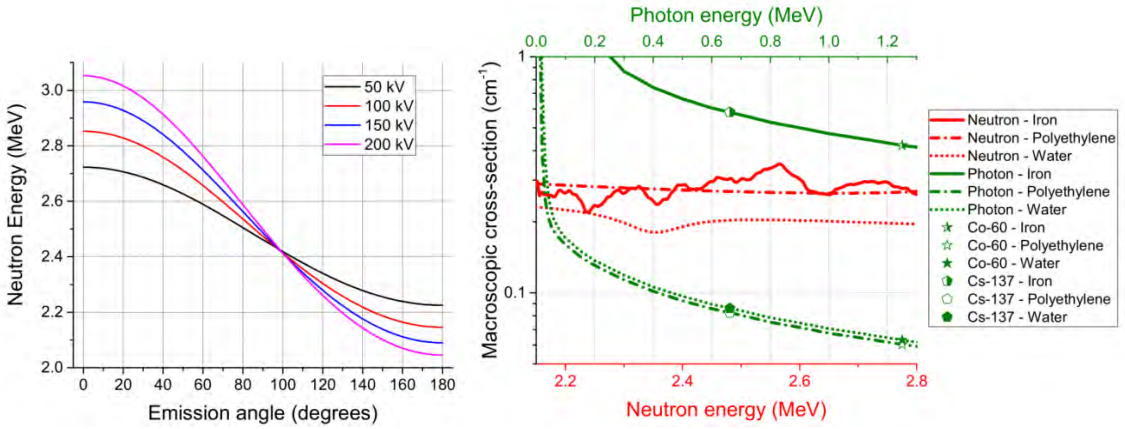

Figure 1. Neutron energy vs. emission angle for different deuterium acceleration voltages (left) and the macroscopic attenuation coefficients for neutrons and photons for example materials in the energy regions of interest (right).

Compared to the more commonly used X-rays and gamma imaging techniques, however, fast neutrons suffer from generally very low source outputs which creates challenges in keeping imaging exposure times reasonable. At the Paul Scherrer Institute (PSI) a custom fast neutron generator and detector array is under development with the goal of overcoming this challenge (Adams *et al.*, 2015). The source is intended to have as high an output as possible while keeping the emitting spot small, to avoid excessive image blur. At the same time, fan-beam detector arrays are being developed to perform tomographic imaging with that source. The high penetrating power of fast neutrons, an advantage in some imaging applications, also makes efficient detection difficult. In the following sections, the development of this custom source and detector array is described, along with tomographic tests and first efforts towards using such a setup for element-sensitive imaging.

2 NEUTRON GENERATOR DEVELOPMENT

Fast neutron generators based on the D-D reaction typically use an ion source from which deuterium are extracted and accelerated electrostatically towards a target with high negative bias voltage on the order of -100 kV. The PSI neutron generator uses an RF-driven plasma ion source at ground potential from which a pulsed extraction electrode (typically -3 kV) pulls deuterium ions. The ions are accelerated towards a titanium target which can be operated up to -150 kV, based on the currently used power supply, but is typically operated at roughly -90 kV to avoid voltage breakdown. Unlike most commercially available neutron generators, the PSI neutron generator target rod is oriented perpendicularly to the ion beam to allow placement of imaging objects close to the source (~10 cm minimum), in order to use a large solid angle of the few emitted neutrons in a fan-beam imaging arrangement. Neutrons are emitted in all directions from the emitting spot but using the forward direction for imaging also takes advantage of the forward bias of the neutron output, roughly 2x the average over 4π. The so-called drive-in target is loaded with deuterium (forming TiD_x where x is theoretically up to 2) by the ion beam itself, which at the same time initiates fusion reactions. The ion extraction is pulsed typically at 3 kHz, with the extraction duty factor used to control the average ion beam current, with typical duty factor operation up to about 50%. The total average beam current, measured by the target high voltage power supply, is typically up to about 0.9 mA. The emitting spot was simulated and measured to be approximately 2 mm for the initially used non-rotating target arrangement. A schematic of the neutron generator design can be seen in Figure 2.

2.1 Rotating beam target

Heat removal from the beam target is of critical importance in maintaining a high neutron output because deuterium outgasses from the titanium target at approximately 200˚C. The first target design was solid titanium without active cooling. This was later upgraded to air cooling, then deionized water (to avoid conductivity to ground) cooling, to improve performance. Due to the desired very high power density (~kW/cm^2, the same order of magnitude of an arc welder), the non-rotating target with active cooling was still observed to severely overheat, as indicated by visible oxidation and a saturation, followed by decline, of neutron output with increasing high voltage (i.e., beam power), whereas the

theoretical yield should monotonically increase with high voltage and power over the energy range of interest.

The non-rotating target could be operated stably for many hours at approximately 7E6 neutrons/s output. The aforementioned heating limitation motivated the design and implementation of a rotating beam target (Kromer *et al.*, 2018). The peak temperature could have been decreased by modifying the design to have a larger beam spot area, and therefore power density, but this would compromise the imaging resolution performance. A rotating target allows effectively distributing the small beam spot heat deposition over a ring around the target, lowering peak temperature. The non-rotating target had a solid titanium layer of about 0.5 mm thickness between the incoming beam and the water cooling. Compared to, for example, copper, titanium is a very poor conductor of heat. The rotating design, therefore, was designed to be made of copper with a thin coating of titanium of approximately 5 micron, produced by physical vapor deposition. Titanium is generally used as a target material due to its high capacity for deuterium loading and relatively low-Z compared to most common metals, meaning that the deuterium slowing down in the target has a relatively lower energy loss in the host metal compared to the implanted deuterium.

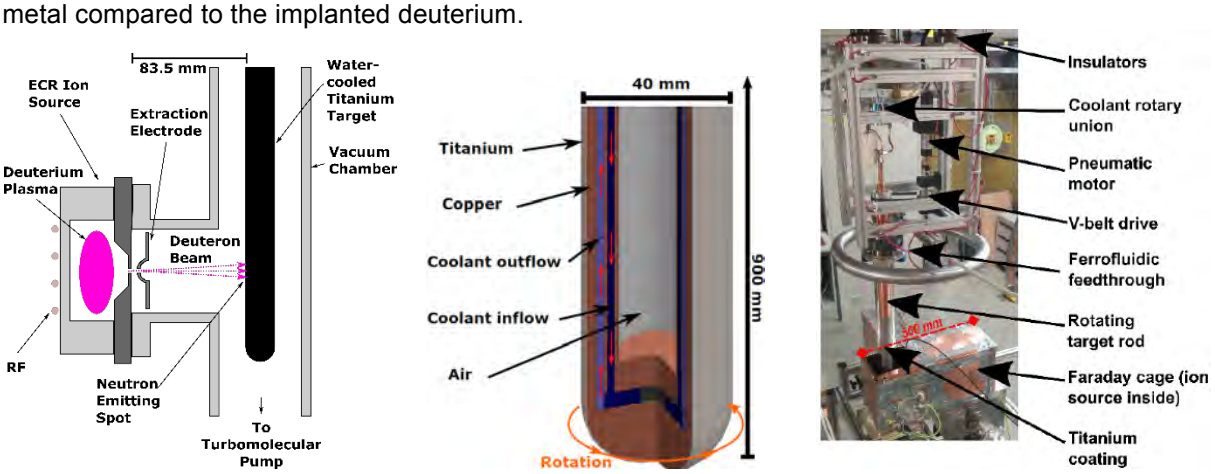

Figure 2. Schematic of D-D generator operating principles (left), drawing of rotating beam target (middle), and photo of rotating target setup (right).

The rotating target design was based on extensive computational fluid dynamics (CFD) and heat transfer simulations using COMSOL Multiphysics 5.2a. It consists of essentially three copper tubes forming two annular cooling channels, one channel for incoming coolant and one for outgoing. A drawing of this geometry is seen in Figure 2, along with a photo of the main components of the rotating target. The inner region of the target is hollow (ambient air) to reduce parasitic attenuation of neutrons in the forward (imaging) direction from the emitting spot. The target rod is inserted into the vacuum chamber via a rotating ferrofluidic feedthrough. The inlet and outlet water lines are connected to a secondary two-channel coolant rotary union in ambient air above the vacuum chamber. This allows the target rod and its two coolant lines to freely and continuously rotate without the two lines wrapping around one-another.

Simulations indicate that with the rotating target arrangement implemented, the peak surface temperature at typical operating beam power is well below the outgassing temperature even for modest rotating speed. This is shown in Figure 3. The power supply currently used is theoretically capable of about 300 W of beam power (2 mA at -150 kV). According to simulations, the typical operating rotating speed of about 60 rpm keeps the peak temperature well below the outgassing temperature at this power limit. Current typical operation, as previously mentioned, is at about 80 W (roughly -90 kV and 0.9 mA). Operation at this power level was found to not produce any visible oxidation in the target surface, and furthermore the neutron output increased monotonically with beam power as theoretically expected, further indicating that the outgassing temperature was not reached. With the rotating target, steady operation was maintained at approximately 3E7 neutrons/s, about four times more than for the non-rotating target. The operating power was limited by the voltage breakdowns previously mentioned and the current which could be extracted from the plasma through the ~1 mm diameter aperture. It is expected that improvement of either of those limits would increase the output further without overheating it, based on the results so far and the simulations.

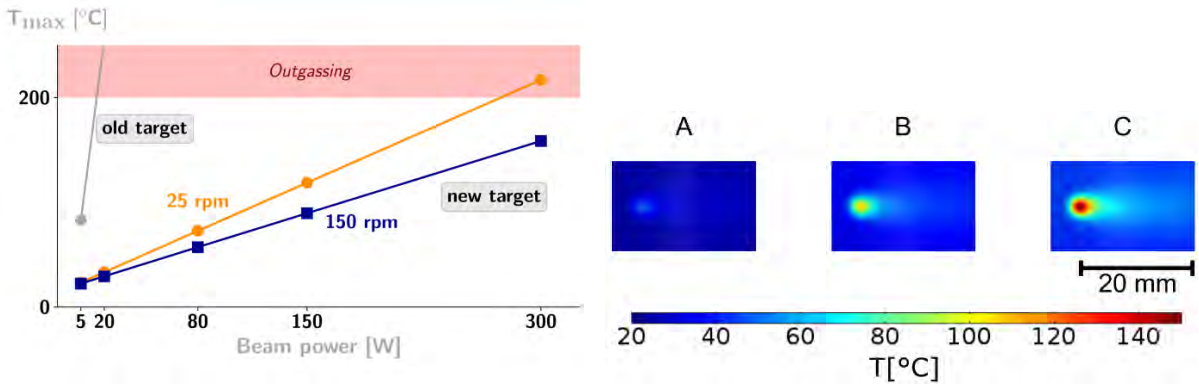

Figure 3. Maximum temperature for different rotation speeds and beam powers (left), and surface temperature distributions (right) for 220 RPM at 70 W (A), 200 W (B), and 300 W (C)

2.2 Characterization measurements

The previously mentioned neutron outputs were estimated using a Berthold LB6411 neutron probe. The detector response was related to neutron output using a detailed Monte Carlo simulation of the source and room geometry, and source emission characteristics, considering also scattering and the energy-dependence of the detector. It is planned to validate this further with indium foil activation measurements. The more challenging parameter to experimentally validate is the emitting spot size, as direct measurement is not practical. The previously mentioned 2 mm emitting spot size for the non-rotating target was determined using ion beam optics simulations (Zboray *et al.*, 2014) along with an edge spread measurement (Adams *et al.*, 2015). The edge spread measurement consisted of moving an attenuating edge step-wise between the source and a plastic scintillator used as a neutron counter, while measuring the neutron count rate. This is illustrated in Figure 4. The edge spread function as measured by the detector is a convolution of the emitting spot size, the edge thickness, and the detector width. Monte Carlo simulations were used to relate the emitting spot size to the edge spread response for a given measurement geometry. This is planned to be repeated for the rotating target, which may have a different emitting spot size due to the shorter ion source to target surface difference (and therefore different beam optics characteristics).

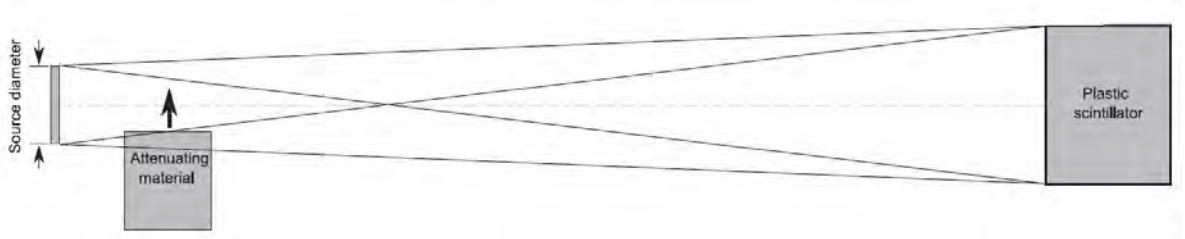

Figure 4. Schematic of edge spread measurement to determine emitting spot size.

3 IMAGING DETECTOR ARRAY

The initial prototype detector array had a relatively coarse detector pitch and slow readout electronics. A second-generation fast neutron detector array is being developed upon this basis, with a finer detector pitch and far more powerful, flexible, and modular readout electronics. The second-generation system is currently being implemented at first for gamma tomography, but the electronics are applicable to a planned fast neutron detector array by changing the scintillation material. These two systems, and the results obtained so far, are detailed in the following sub-sections.

3.1 Prototype detector array

The first-generation detector array consists of about 100 individual detectors arranged in a fan-beam arc at a distance of 100 cm from the source (Adams *et al.*, 2014). A schematic of the arrangement can be seen in Figure 5. Each detector consists of a plastic scintillator read out by two Silicon photomultipliers (SiPMs) in parallel (two were used to increase light collection area, though they function essentially as one). The signal was amplified and then discriminated at a level set by a

potentiometer on each individual detector pulse-processing board (one per detector) which cuts all parasitic X-rays coming from the source while counting as many fast neutrons, elastically scattering with hydrogen in the scintillator, as possible. Counting was done via a latching circuit which allowed ~20 channels to be read out by a single Arduino Due microcontroller board, but only at low counting rates (order of kHz in total over all 20 channels). Each scintillator was 5 mm wide, had a height of 8 mm, and had a detector pitch of 6 mm. The detector depth was 80 mm in order to achieve a high degree of attenuation of the fast neutron flux in the scintillator. After loss of efficiency due to the discrimination threshold, the overall detection efficiency was about 35% of the neutron flux incident on the detector face. A photo of the setup can be seen in Figure 5.

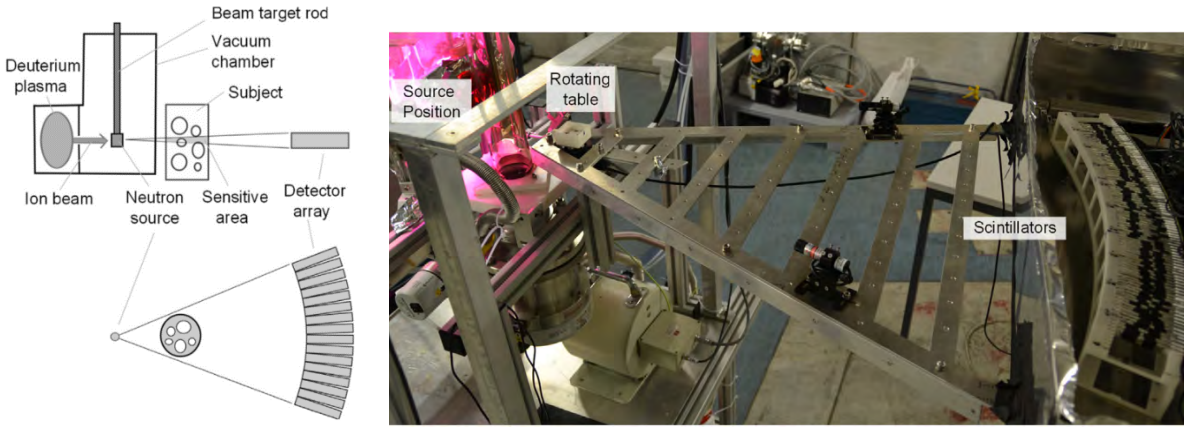

Figure 5. Schematic of imaging setup (left) and a photo of the prototype detector array (right).

3.2 Second generation detector array

The second-generation detector array is based on an 8-detector modular approach (Adams, Petrov and Manera, 2017). A 3D printed scintillator holder allows for a 2.5 mm detector pitch, and is currently implemented with a scintillator height of 8 mm and a depth of 15 mm. The scintillator holder also accommodates a SiPM-holder board, again with two SiPMs operating in parallel for each scintillator. The SiPM-holder board is connected via 8 RF cables (one for each scintillator detector) to an amplifier/discriminator board, which is in turn connected to a counter board. A microcontroller board is plugged into the counter board. An overview schematic is shown in Figure 6.

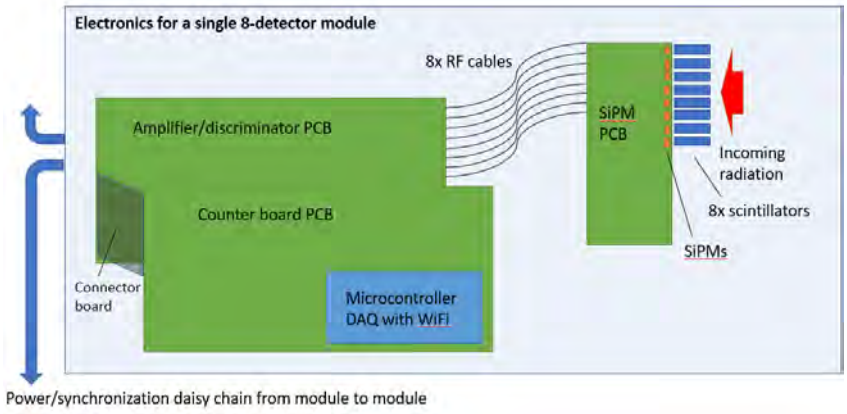

Figure 6. Schematic of 8-detector module.

Each individual detector signal is amplified and then goes to two discrimination and counting lines each in order to have an upper and lower energy threshold. A schematic of the pulse processing chain of a single detector can be seen in Figure 6. The difference in counts between the two thresholds for a given detector corresponds to an energy window of interest. Each channel (two per detector) has a 16-bit counter, and all counters on a given module are on a shared readout bus. The counts values are read out and saved by a microcontroller with WiFi capabilities, a process which takes about 20 ms per readout of the module. At the end of a measurement series (practically unlimited number of time

steps) the data can be transferred to a PC. A schematic of an individual detector pulse-processing chain can be seen in Figure 7.

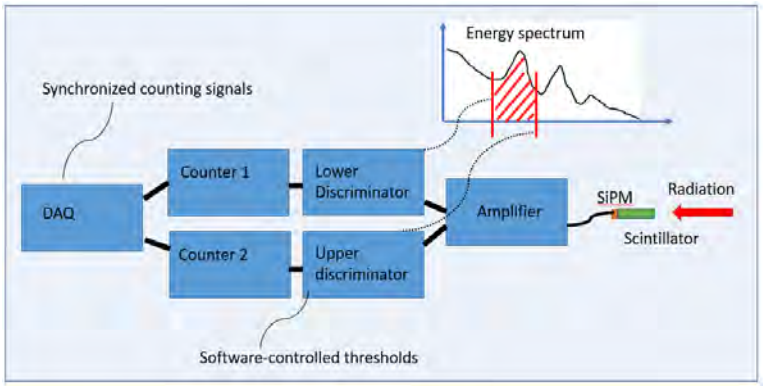

Figure 7. Schematic of pulse processing chain for a single detector.

All modules of an array are connected together on a daisy chain via the counter board. This daisy chain consists of ground, SiPM bias, 12V to power the pulse-processing boards, an I2C bus for setting the discrimination thresholds, and shared store/clear/record TTL signal lines for the counters. The I2C bus allows software-controllable individual thresholds to be set for each detector. The store signal causes counter values to be internally stored to the counter integrated circuits, without disrupting counting (i.e. no dead time). The clear signal sets all counters back to zero. The record signal goes to the microcontroller board, initiating the bus readout process, again without disrupting counting (although requiring the aforementioned 20 ms before it is ready for readout of a new time step). Having hard wiring of the store/clear/record signals, rather than software control, ensures robust timing synchronization of all detector channels. Photos of the 3D printed scintillator holder and the various electronics boards can be seen in Figure 8.

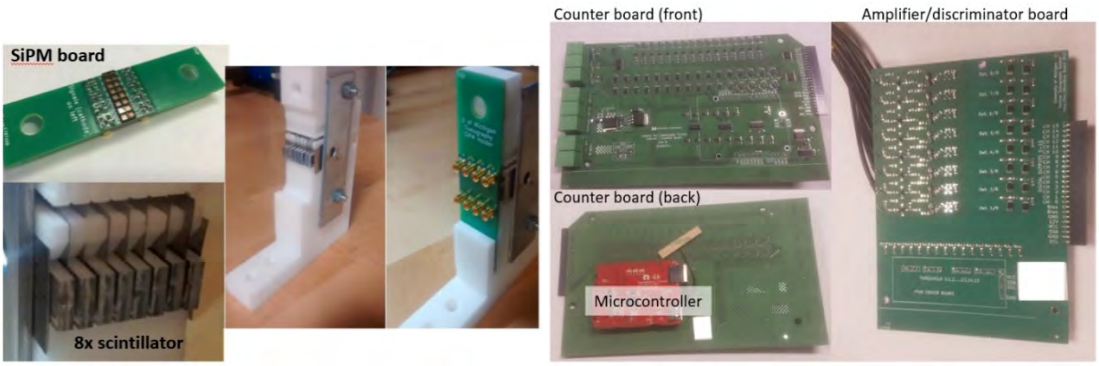

Figure 8. Photos of second-generation 8-detector module scintillator holder, SiPM-holder board, and readout electronics boards.

This modular approach is being applied at first to gamma imaging with an Ir-192 source (Diaz *et al.*, 2018) and is planned to later be used in a second similar array for fast neutron imaging. The only difference will be the choice of scintillator, LYSO for gamma detection and plastic scintillator for fast neutrons, but otherwise the readout electronics are suitable for both.

3.3 Experimental imaging results

Test imaging results of a Siemens star test object can be seen in Figure 9 (Adams, Zboray and Prasser, 2016). This includes fast neutron and Co-60 tomograms of a plastic Siemens star test object with a 1 cm thick stainless steel casing around it, produced with the prototype neutron detector arc and the non-rotating target. The difference in contrast in the plastic region illustrates the difference between photon and fast neutron imaging in such a scenario with plastic shielded by steel. The Siemens star periodicity was used to estimate an imaging spatial resolution of about 2 mm, which agreed with simulations as well as a tomogram of a square object used to produce an edge spread

function. The total exposure time for the fast neutron imaging measurement was approximately one hour.

The first imaging tests with the second-generation setup were performed with a single 8-detector module and an Ir-192 gamma source. The 8-detector module was placed on a linear stage such that it could be automatically moved from one “module position” to another, simulating a multi-module detector array. The same plastic Siemens star test object was imaged in a fan beam imaging arrangement, resulting in an effective spatial resolution of about 1 mm, again agreeing with simulations. The exposure time was approximately one hour for both prototype detector array images in Figure 9, performed with the non-rotating beam target (expected to be approximately 4x slower than the rotating target output).

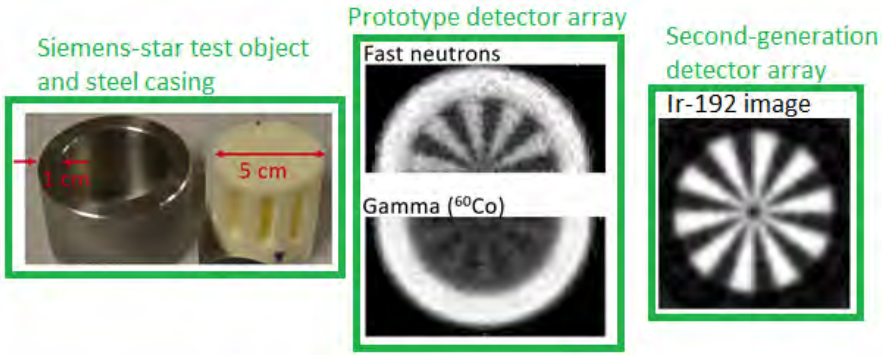

Figure 9. Photo and tomographic images produced by the prototype and second-generation detector array.

A bulkier sample was also investigated with the prototype detector array. This consisted of a 30 mm thick steel ring with an outer diameter of 190 mm, in which three 40x40 mm^2 blocks were placed, one each of aluminium, plastic, and steel. The exposure time was approximately four hours (again with the non-rotating target, this would be expected to be approximately 4x faster with the rotating beam target). The theoretical attenuation value images are shown in Figure 10, along with simulated images and experimental ones, for both fast neutrons and a Co-60 gamma source. The simulations were performed by forward-projecting the theoretical image, adding noise according to the experimental measuring time and expected detector count rates, and then applying a filtered back-projection. This was intended to investigate whether the image contrast and quality would compare well with the experiments. Except for some ring artefacts, due to several malfunctioning detector channels, the agreement was qualitatively good. This gives confidence in using comparable simulations with any other object geometries to estimate imaging performance. Furthermore, the fast neutron images show very good contrast compared to the Co-60 images in the internally located blocks of material despite being shielded by 3 cm of steel.

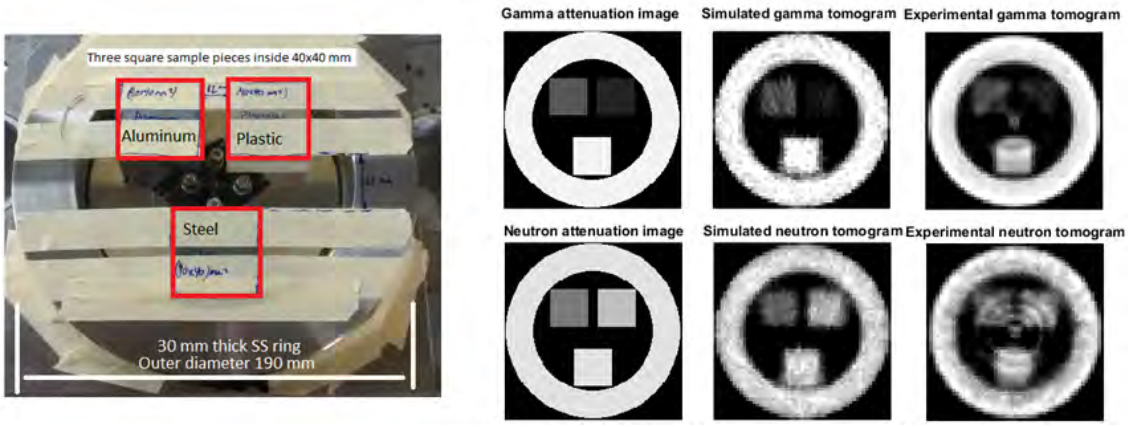

Figure 10. Sample object photo (left), theoretical attenuation image, simulated tomogram, and experimental tomogram for both Co-60 and fast neutrons (right).

A complete second-generation gamma detector array has been assembled and is in early stages of testing with an Ir-192 source. It consists of 240 detectors in total (30x 8-detector modules) with an 800

mm source to detector distance. Measured spectrum data have confirmed basic functionality of the scaled-up system, and a graphical user interface is used to remotely set discrimination thresholds and to collect data. A photo of this setup can be seen in Figure 11. In addition, a single 8-detector module with plastic scintillators (rather than LYSO) was tested with the PSI neutron generator to confirm its suitability for fast neutron imaging. Basic tests were successful, with a roughly 10% detection efficiency of incoming radiation, based on good signal pulse height for easy discrimination of neutron events above the electronic noise and parasitic X-ray background.

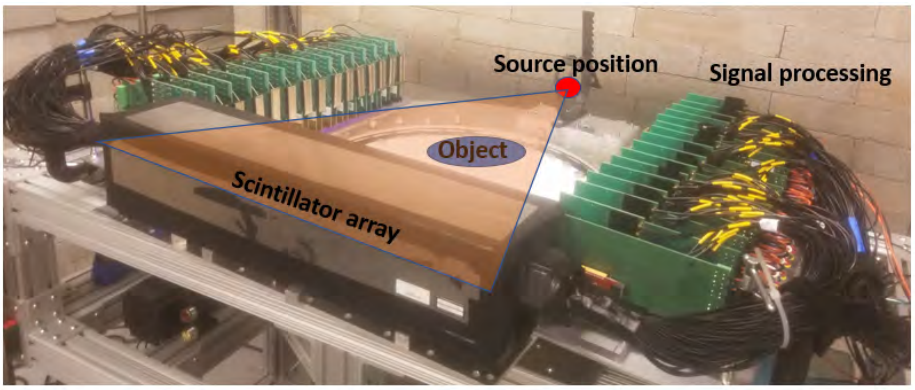

Figure 11. Completely assembled next-generation detector array to be applied to Ir-192 imaging.

4 ENERGY-SELECTIVE TECHNIQUES

As previously described, fast neutron generators have a quasi-monoenergetic output which depends on emission angle. The combination of tomography data, i.e. local attenuation coefficients, from multiple energies can be theoretically combined to differentiate one material from another. For most applications this quasi-monoenergetic emission can be considered as monoenergetic, but when searching for small differences in object attenuation, the slightly polychromatic nature at a given angle becomes non-negligible.

This angle-dependent energy blur is a result of the incoming deuterium ions slowing down in the target and having a continuous chance of fusion from its incoming energy down to zero as it slows down. This blur depends on the deuterium distribution within the target, not known precisely in the PSI neutron generator. Furthermore, the finite solid angle of any real-world detector blurs the effective emission angle, and therefore the energy distribution. The extreme cases of target loading are a Dirac delta function where all fusion reactions occur at exactly the acceleration energy, and the case where the target is fully loaded with TiD_2. Simulations were performed to estimate the resulting angle-dependent spectra for these two cases, and an intermediate case referred to as round peak. With this basis of comparison, measurements were performed with simple, homogeneous samples in order to determine whether the theoretical attenuation coefficients could be reproduced with neutron generator measurements (Soubelet *et al.*, 2018).

4.1 Experimental setup

In order to measure at a range of angles from 0 to 180 degrees, a goniometric mechanical structure was fabricated. It consists of an arc-shaped table with gears, on which a trolley can be remotely moved around the arc. On the trolley are several plastic scintillator detectors identical to the prototype detectors previously described, functioning as a single neutron counter. Monte Carlo simulations of the experimental setup were used to subtract estimated room-scatter from the measured counts values. Three measurement series were performed for each sample, one with no object, one with a sample of known thickness entirely covering the detectors, and one with a blinding cone blocking more than 99% of direct neutron flux. The combination of these three measured datasets were used to calculate the attenuation of the sample at a range of angles. A drawing and photo of the experimental setup can be seen in Figure 12.

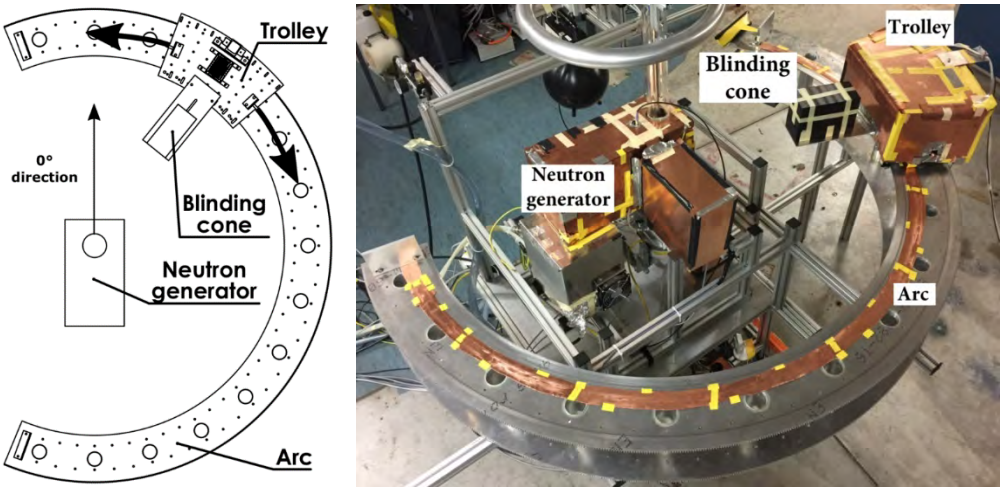

Figure 12. Drawing of arc and trolley setup from above (left) and photo of the setup (right).

4.2 First measurements

Experimental results for two samples, alumina and magnesia, with particularly distinct attenuation vs. angle curves are shown in Figure 13, as compared to the three simulated curves assuming different target loading profiles. The experimental curves qualitatively followed the theoretical ones well, but with some deviation. This deviation might be due some combination of uncertainties in the loading curve, the theoretical attenuation values, and the neutron scattering in the experimental setup. The fundamental emission angle dependence of sample attenuation, however, was well represented.

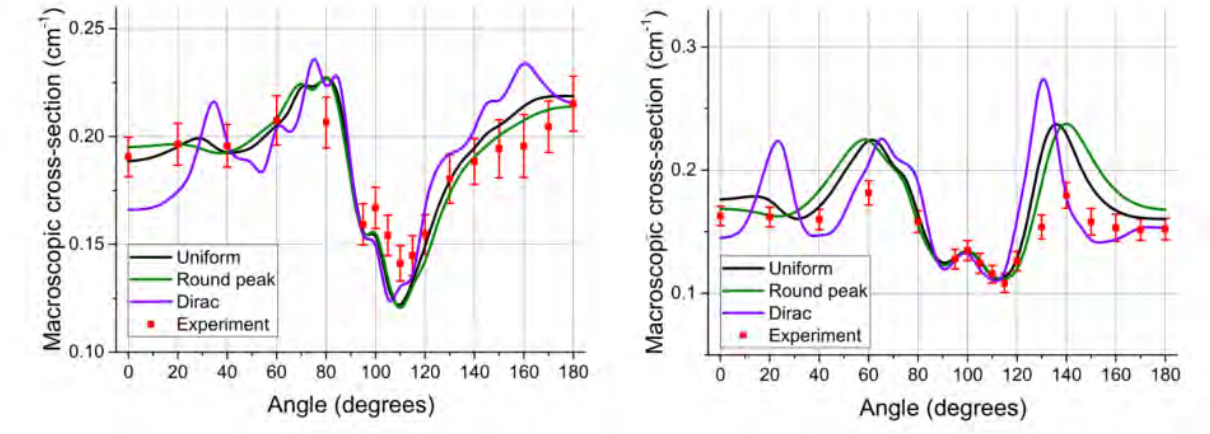

Figure 13. Experimental attenuation curves compared to simulated ones for three loading profiles for alumina (left) and magnesia (right).

5 CONCLUSIONS AND OUTLOOK

The current state of the PSI fast neutron generator was described. Implementation of a rotating beam target resulted in a roughly 4x increase, compared to the non-rotating target, in neutron output to 3E7 neutrons/s over 4π. Further characterization of the emitting spot will be performed. The RF-driven ion source is in the process of being upgraded to a microwave-driven ion source, which is hoped to increase the maximum beam current. A planned improved vacuum chamber design, combined with the change to a microwave ion source, is furthermore expected to increase the voltage breakdown limit, allowing for higher target voltage and therefore higher beam power and output.

Imaging results with the prototype detector array showed the capability of the system to perform tomographic imaging. The second-generation detector array with 8-detector modular readout electronics, tested at first with an Ir-192 gamma source and LYSO scintillators, is planned to be

implemented with plastic scintillators for fast neutron imaging. This is expected to improve the imaging spatial resolution from about 2 to 1 mm.

The first steps of energy-selective fast neutron tomography with a compact neutron generator were also performed, including source emission angle dependent attenuation measurements of homogenous samples. Measurements with a series of other samples are being performed in order to produce reference setup-specific attenuation curves for a range of elements. The tomographic imaging simulation approach tested with a single energy are planned to be applied to more realistic samples of interest, such as those containing both oil and water, to evaluate element-sensitivity capabilities. This should give information about which applications the technique might be effective for, and the limitations of the approach in contrast.

Besides distinguishing oil from water (difficult or impossible with traditional techniques), it is also planned to explore whether hazardous elements can be identified in unknown samples. Examples include arsenic and chlorine, components in chemical weapons, which might be present in unknown quantities in unexploded ordnance. The good low-Z contrast of materials shielded by high-Z material exhibited by fast neutrons is also considered for application to multi-phase fluid dynamics studies in high-pressure nuclear fuel bundle mock-ups, such as determining void fraction distributions of small quantities of water in the presence of thick metal structures.

REFERENCES

ADAMS, R. et al. (2014) ‘Conceptual design and optimization of a plastic scintillator array for 2D tomography using a compact D–D fast neutron generator’, Applied Radiation and Isotopes, 86, pp. 63–70. doi: 10.1016/j.apradiso.2014.01.001.

ADAMS, R. et al. (2015) ‘Development and characterization of a D-D fast neutron generator for imaging applications.’, Applied Radiation and Isotopes, 96, pp. 114–21. doi: 10.1016/j.apradiso.2014.11.017.

ADAM, R., PETROV, V. and MANERA, A. (2017) ‘Advanced Radiation-Based Imaging Techniques for Detailed Void Fraction Measurements in High-Pressure Flow Loops’, in NURETH.

ADAMS, R., ZBORAY, R. and PRASSER, H. M. (2016) ‘A novel fast-neutron tomography system based on a plastic scintillator array and a compact D-D neutron generator’, Applied Radiation and Isotopes. doi: 10.1016/j.apradiso.2015.09.002.

DIAZ, J. et al. (2018) ‘High Resolution Gamma-Ray Tomography Imaging for Detailed Void Fraction Measurements in High-Pressure Flow Loops’, in Advances in Thermal Hydraulics (submitted).

KROMER. H. et al. (2018) ‘Thermal analysis, design, and testing of a rotating beam target for a compact D-D fast neutron generator’, Applied Radiation and Isotopes (submitted).

SOUBELET, B. et al. (2018) ‘Feasibility study of using a compact deuterium-deuterium (D-D) neutron generator for energy-selective transmission tomography’, Journal: Radiation Physics and Chemistry (submitted).

ZBORAY, R. et al. (2014) ‘Development of a fast neutron imaging system for investigating two-phase flows in nuclear thermal–hydraulic phenomena: A status report’, Nuclear Engineering and Design. Elsevier B.V., 273, pp. 10–23. doi: 10.1016/j.nucengdes.2014.01.027.